

An integrated 3D sound intensity sensor using four-wire particle velocity sensors: II. Modelling

This article has been downloaded from IOPscience. Please scroll down to see the full text article.

2010 J. Micromech. Microeng. 20 015043

(<http://iopscience.iop.org/0960-1317/20/1/015043>)

The Table of Contents and more related content is available

Download details:

IP Address: 130.89.19.9

The article was downloaded on 28/01/2010 at 12:59

Please note that terms and conditions apply.

An integrated 3D sound intensity sensor using four-wire particle velocity sensors: II. Modelling

J W van Honschoten, D R Yntema and R J Wiegerink

Transducers Science and Technology Group, MESA⁺ Research Institute, University of Twente, PO Box 217, 7500 AE Enschede, The Netherlands

E-mail: j.w.vanhonschoten@ewi.utwente.nl

Received 3 July 2009, in final form 23 October 2009

Published 14 December 2009

Online at stacks.iop.org/JMM/20/015043

Abstract

The sensitivity of a micromachined acoustic sensor consisting of four hot-wire particle velocity sensors is analysed theoretically and experimentally. The device and its fabrication have been presented in part 1 of this paper (Yntema *et al* 2010 *J. Micromech. Microeng.* **20** 015042). A relatively straightforward analytical model is presented that describes both the air flow around the probe and the temperature profile around the heated wires. The presence of the chip surface near the heated wires influences the fluid flow around the wires, while it also affects the temperature distribution in the probe by altering the direction of heat transport. Both effects result into a modified angular dependence of the sensor sensitivity with respect to the normal 'figure-of-eight' figure of the response. By means of finite elements software, the thermal and the acoustic flow behaviour of the sensor are also investigated numerically, both effects together and each apart, and the results are compared to the analytical model. Comparison with the experimental data is presented, showing that the model is appropriate to describe the angular dependence and the magnitude of the sensor response. It is concluded that the perturbed air flow due to the chip surface is the dominant reason for the observed angular sensitivity.

1. Introduction

In the acoustical practice, during the last few decades the study of vector fields and acoustic flow has become of increasing interest. Next to the acoustic pressure, the acoustic particle velocity can be measured experimentally nowadays, allowing for a much more effective way of characterizing sound fields, visualizing acoustic flows and investigating real-life energetic effects of acoustic power flow (such as scattering, vortex flow, shielding area, etc) than with pressure measurements only. By means of a particle velocity sensor complementary to the conventional pressure microphone, a complete characterization of the three-dimensional sound field, including the intensity streamlines and the different contributions of the sources, becomes possible. A micromachined hot-wire particle velocity sensor for this purpose, composed of two parallel heated wires, was presented about 10 years ago by De Bree [2–4]. Until then, most flow sensors were based on a single hot-wire

anemometer concept. Anemometers, however, are not linear, not sensitive to small velocities and, in particular, not directional [5, 6]. Since its introduction, the particle velocity sensor has been mainly used for measurement purposes, in particular broadband one- and three-dimensional sound intensity measurements [7–10] and the determination of acoustic impedances, *in situ* or otherwise [11]. Its sensitivity behaviour and characteristics have been studied extensively [12–15], while it has been further developed and improved, for example to a three-wire configuration, with a higher signal-to-noise ratio.

Thanks to their direction-dependent sensitivity, particle velocity sensors are valuable in the separation of many uncorrelated sound sources and estimating the contributions of these sources to the total sound field [16–21], whereas the noise level of the sensor response can be significantly reduced [15]. When the contribution of each sound source to the total sound field is known, techniques with array applications such as direct sound field measurements or inverse acoustics can

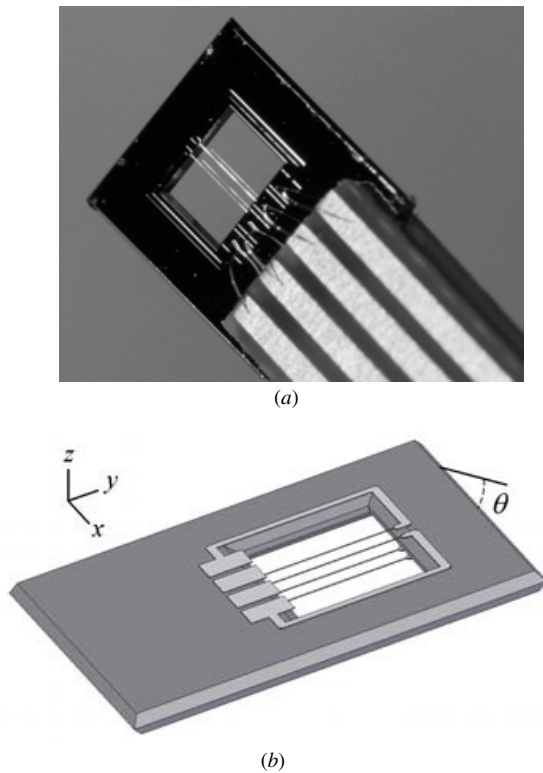


Figure 1. (a) The four-wire particle velocity probe, containing four 1 mm long sensor wires suspending the rectangular orifice in the chip surface. (b) Schematic drawing of the probe. The distance between the wires is 250 μm .

be applied for each source. Especially in near field acoustic holography [22, 23], where the sound field is measured in close proximity to the vibrating object, particle velocity measurements allow for distinguishing the multiple sources from noise sources.

In the preceding paper, ‘An integrated 3D sound intensity sensor using four-wire particle velocity sensors: part 1’ [1], an integrated particle velocity sensor with omni-directional sensitivity was presented [14, 24–26], consisting of four individual particle velocity sensors integrated on a single silicon die. This integrated design allowed the realization of three-dimensional sensitive acoustic sensors with very good reproducibility in terms of directional sensitivity.

From the above it will be clear that, for a very accurate determination of the direction of the involved particle velocities, a good understanding of the directional sensitivity of the probe is needed. However, the current designs show a deviation in their directional sensitivity pattern from the ideal ‘figure-of-eight’ response [3] that would be the case for free standing wires. Up to now, this deviation has not been fully understood. The purpose of this paper is to analyse this effect and model the directional sensitivity pattern for the four-wire probe (see figure 1), with the sensor wires placed within a square orifice in the chip surface. Contrary to a previous analysis [26] which focussed on the flow pattern around the sensor, in this paper all important physical aspects are taken into account. Namely, we consider both the acoustic flow profile around the device, that is disturbed due to the presence

of the printed circuit board acting as a disturbance for the flow, and the local temperature distribution around the wires. As will be shown, the chip surface acts as a heat sink that affects the heat transport due to convection. Consequently, it influences the directionality of the sensor response to particle velocities.

2. Theory

Ideally, the two parallel heated wires of a particle velocity sensor exhibit a $(\cos \theta)$ -dependent response to a fluid flow imposed under an angle θ with respect to the plane of the wires since the sensor wires detect the velocity component directed in the plane of these wires only. This $\cos \theta$ angular dependence on the incoming flow is sometimes referred to as a ‘figure-of-eight’ response, related to the representation of the sensor response in the polar plane [3, 7, 8, 14]. However, in practice free standing wires without any connections to the probe do not exist, and as a consequence of the surrounding material the angular dependence of the sensitivity is significantly influenced. For the probe as shown in figure 1, where the thin wires (1 mm long, 300 nm thick silicon nitride beams with a 100 nm platinum/chromium layer on top) are placed within a square orifice in a 250 μm thick silicon support, measurements show that the figure-of-eight pattern is rotated by 10–20° due to the presence of the silicon substrate [1]. That is, the angle θ of the incoming flow is rotated by 10–20°, independent of θ itself.

In the experiments it is not only seen that the measured angle deviates from the angle θ of the incoming flow, this angular shift appears to be θ -independent as well, which results in a constant rotation of the entire ‘figure-of-eight’ curve of $18 \pm 2^\circ$ in the polar plane. For a slightly different version of the probe, with an integrated pressure microphone [1], this deviation is measured to be $13 \pm 2^\circ$.

There are two possible causes for this observed effect. First, the presence of the chip surface in the proximity of the wires is likely to have a disturbing effect on the air flow, thereby altering the direction of the local velocity at the position of the wires. Second, the silicon surface may act as a heat sink resulting in a disturbance of the temperature distribution around the heated sensor wires. In the remainder of this section, both phenomena are investigated. First, we deduce an expression for the temperature in the probe and analyse the consequences, next we calculate the stream profile of the air in and around the probe, and finally we combine these effects.

2.1. The temperature around the wires

To analyse the response of the sensor due to an imposed acoustic flow, the temperature profile around the heated wires has to be calculated. At first, the static temperature distribution in the device is calculated, when no air flow is present. An acoustic wave gives only a small perturbation to this temperature profile and the output signal of the sensor is linearly proportional to the local temperature gradient at the position of the sensor wires [12, 13, 26]. Therefore, the

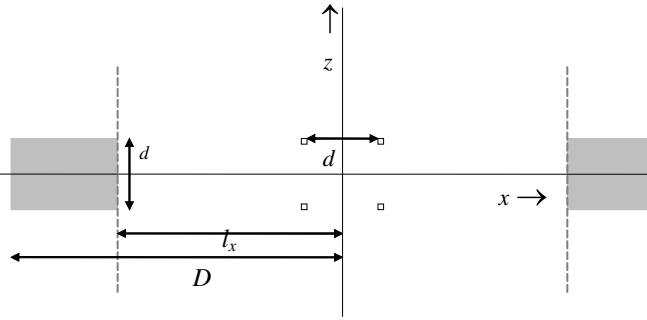


Figure 2. Cross-sectional view of the model geometry for the calculation of the temperature distribution. The thickness of the substrate (the chip) is d ; its full width is $2D$, the horizontal distance between the wires is also d . In writing the expansion (6), it was assumed that the walls at fixed temperature $T = 0$ extend to infinity, as illustrated by the dotted lines.

static temperature distribution provides sufficient information to deduce all relevant sensitivity properties, in particular to obtain the angle of maximum sensitivity of the device.

In the absence of air flow and when the wires are heated by a constant electrical current, the temperature distribution around the wires follows from the stationary heat equation

$$-\vec{\nabla}(k\vec{\nabla}T) = Q, \quad (1)$$

where $k = k(T)$ is the thermal conductivity of air, which is in principle a function of temperature, and Q represents the heat produced by the heater per unit volume per unit time. Since Q is nonzero only at the heated wires (i.e. at $(x,z) = (\pm x_0, \pm z_0)$), it can be written as

$$Q = \frac{P}{l_y} (\delta(x - x_0) + \delta(x + x_0)) (\delta(z - z_0) + \delta(z + z_0)), \quad (2)$$

where P is the dissipated power in the wire and l_y is the wire length. In general, the heating power is not distributed uniformly over the wire because the local resistance is temperature dependent; however, the variation along the wire is only a few per cent and can therefore be neglected. The coordinate dependence of the heat sources is described by Dirac delta functions since the heater thickness h and width w (400 nm and 5 μm , respectively) are small with respect to the other dimensions of the device and can thus be neglected in calculating the temperature distribution [12, 13].

As illustrated by the cross-sectional view in figure 2, the four wires are located at $(x, z) = (\pm d/2, \pm d/2)$. On the surface of the silicon substrate, the temperature and the heat flux have to be continuous, that is,

$$T = T_s, \quad k \frac{\partial T}{\partial n} = k_s \frac{\partial T_s}{\partial n}, \quad (3)$$

with T_s and k_s the temperature and thermal conductivity of the substrate, respectively. Due to the high thermal conductivity of silicon, the ratio $k/k_s \approx 1.6 \times 10^{-4}$ is small and the temperature gradient inside the substrate can be neglected, so that the boundary condition is simplified to

$$T = T_0, \quad (4)$$

with T_0 the room temperature. Let us assume first that k does not depend on temperature. Further we assume that the leakage of heat power to the substrate via the beam ends is small compared to the total dissipated power. This last assumption will be checked below.

Then, the heat equation (1) becomes linear:

$$\partial_x^2 T + \partial_y^2 T + \partial_z^2 T = -\frac{P}{l_y} \left(\delta\left(x - \frac{d}{2}\right) \delta\left(x + \frac{d}{2}\right) \right) \cdot \left(\delta\left(z - \frac{d}{2}\right) \delta\left(z + \frac{d}{2}\right) \right), \quad (5)$$

and one can easily shift the temperature T to $T - T_0$, so that the boundary conditions become $T = 0$ on the chip surface and $T \rightarrow 0$ for $x \rightarrow \pm\infty$.

For the actual geometry of the device it is difficult to solve this equation analytically. However, we can simplify the geometry by assuming that the walls at $x = \pm l_x$, acting as heat sinks and on which the boundary condition $T = 0$ applies, extend to infinity along the z -direction (see the dotted lines in figure 2). For the temperature in the device we can then make an expansion in harmonics:

$$T(\xi, \eta, \zeta) = \sum_{n=0}^{\infty} \sum_{m=0}^{\infty} T_{nm}(\zeta) \cos \lambda_n \xi \cos \lambda_m \eta, \quad (6)$$

$$\lambda_n = \frac{\pi}{2}(2n + 1),$$

where we have introduced the normalized space variables $\xi = x/l_x$, $\eta = 2y/l_y$ and $\zeta = z/l_x$, where l_x is half the gap distance and l_y is the wire length.

Substitution of this expansion into equation (5) yields ordinary differential equations for the coefficients T_{nm} that can be solved easily, taking into account the boundary conditions. With the parameter $\xi_0 = \zeta_0 = d/2l_x$, the solution for these coefficients is

$$T_{nm}(\zeta) = \frac{2P}{kl_y} \frac{(-1)^m}{\lambda_m \sigma_{nm}} \cos \lambda_n \xi_0 (e^{-\sigma_{nm}|\zeta - \zeta_0|} + e^{-\sigma_{nm}|\zeta + \zeta_0|}) \quad (7)$$

$$\sigma_{nm} = \sqrt{\lambda_n^2 + (2l_x/l_y)^2 \lambda_m^2}.$$

The resulting expression for the temperature, the double series (6), is a quickly converging expansion that can be calculated easily numerically. For a typical set of parameters the temperature distribution is shown in figure 3. Also depicted in these graphs are the results from numerical simulations as described in section 3. The figures show clearly the sharp peaks at the points $(\xi, \eta, \zeta) = (\pm \xi_0, 0, \pm \zeta_0)$, that flatten out at increasing distance from the heaters. In the lower graph of figure 3, the y -dependence of T along the heaters is seen: along a relatively large distance this temperature is almost constant and the y -dependence in the central part of the heaters can be neglected.

With the obtained expression (7) for the temperature, we can now also verify the assumption of a constant power dissipation P , along y . From the temperature being constant in the middle part of the heater, approximately $|\eta| < 0.7$, one can conclude that the heating power in this region (which is temperature dependent via the wire resistance) is almost constant along the length. Moreover, an estimation for the power leakage δP to the substrate can be made. Since δP is

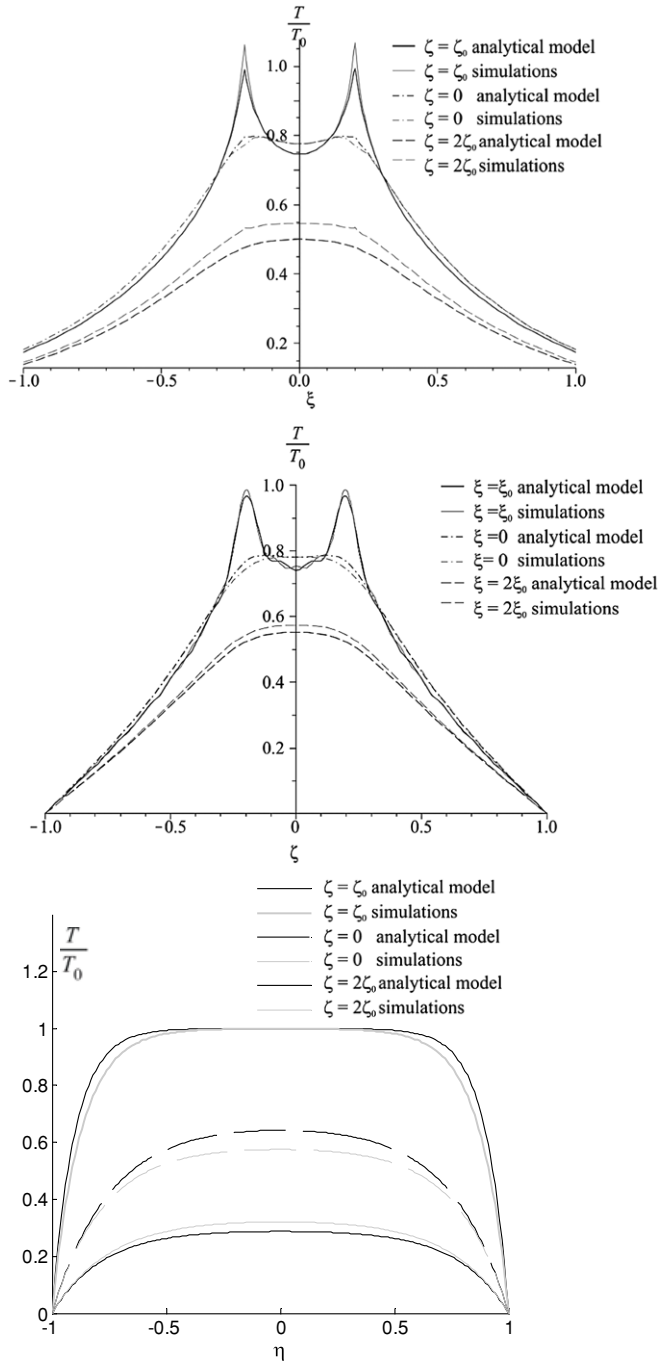


Figure 3. Temperature distribution in the channel along the normalized x - z - and y -axes, respectively, according to the calculated expansion (6) and (7), with $\xi_0 = 0.2$, $l_x = 1$ mm and $l_y = 1.5$ mm. For comparison, results from numerical simulations are also shown. The temperatures were normalized by T_0 , the temperature at the point of the heaters ($\pm\xi_0, 0, \pm\zeta_0$).

the product of the heat flux through the heater ends and the area of the wires cross section,

$$\delta P = 2k_h \left. \frac{\partial T}{\partial y} \right|_{\eta=\pm 1} hw, \quad (8)$$

with h the height of the heated wire, w its width and k_h its thermal conductivity, one can use (7) to deduce $|T/y|_{\eta=\pm 1}$ and evaluate the heat power δP dissipated through the wire ends.

If we use $k_h \sim 18.5$ W m⁻¹ K⁻¹, $k = 0.0263$ W m⁻¹ K⁻¹ and a wire thickness h of 100 nm and width $w = 2$ μ m, we obtain $\delta P/P \approx 0.02$. So, the power leakage to the substrate is relatively small.

The obtained static temperature profile is the required starting point to find the sensitivity of the device and its response to an acoustic gas flow. If due to an acoustic wave the gas close to the heaters moves with a velocity v , the temperature around the wires is described by the full heat equation

$$\rho c_p (\partial_t T + \vec{v} \vec{\nabla} T) - \vec{\nabla} (k \vec{\nabla} T) = Q, \quad (9)$$

where c_p is the gas heat capacity at constant pressure. One can define the thermal diffusion coefficient D as $D = k/\rho c_p$, which is approximately 1.9×10^{-5} m² s⁻¹ for our situation. The convective term is responsible for the difference in wire temperatures.

The small temperature differences between the wires lead to variations in the air density, causing a small vertical flow called free convection. To see if this free convection plays a significant role compared with the acoustically induced forced convection, we should consider the relative magnitudes of the Grashof number (Gr), which is a ratio of buoyance force and viscous force [27], and the Reynolds number. For our case (estimating the wires temperature difference as ~ 0.1 K; a particle velocity $\sim 5 \times 10^{-3}$ m s⁻¹; $T_{\text{heaters}} \sim 400$ K), we find that $Gr/Re^2 \approx 0.02$. So, $Gr/Re^2 \ll 1$, and therefore the natural convection due to the acoustically induced temperature variations can be neglected. The high static wire temperature itself leads to substantial air flow due to free convection, but this air flow is constant and will not be modulated by the acoustic signal.

We assume that the heater power is not too large, so that the temperature dependence of the heat conductivity is negligible, and that the particle velocity v is small. Then, the solution of the complete equation (8) is obtained by the earlier found temperature plus a small correction that is proportional to v . The condition that the particle velocity is small means that it is much lower than the diffusion velocity over a characteristic length l , i.e. $v \ll D/l$. Taking the mutual wire distance l as 250 μ m, the correction to the temperature δT will be small, $\delta T \ll T$, if $v \ll 0.08$ m s⁻¹. This corresponds to an acoustic pressure of 36 Pa. Since this is a large sound level, the temperature correction δT is small and one can write for it the inhomogeneous equation

$$\partial_t \delta T - D \vec{\nabla}^2 \delta T = -\vec{v} \vec{\nabla} T, \quad (10a)$$

with the boundary conditions that $\delta T = 0$ on the walls and at infinity. With θ the angle between the *local* gas flow and the (x, y) -plane, this can be written as

$$\partial_t \delta T - D \vec{\nabla}^2 \delta T = -v \partial_x T \cos \theta - v \partial_z T \sin \theta. \quad (10b)$$

This equation can in principle be solved for δT , if the function T is given. For specific geometries of the particle velocity sensor, this has been elaborated, in [12, 13]. The perturbation δT is then also written as an expansion in harmonics and the coefficients can be calculated explicitly. This expansion is a function of geometric parameters, the frequency, and, in

particular, linearly proportional to v/D . With this, the values of δT around the heaters can be evaluated explicitly. The output signal, S , is proportional to the temperature difference between the wires and follows therefore directly from the two values for δT at the respective places.

In this paper, however, the main point of interest is the angular dependence of the output signal, i.e. the sensitivity as a function of θ , and for this purpose the complete solution for δT is not required.

Nor do we have to take specifically into account the frequency dependence. The frequency enters through the finite heat capacity of the wires, which cannot perfectly follow the air temperature variations. First, the region of interest, 10–1000 kHz, is well below the cut-off frequency of the system, several kHz for the current probe [9, 13], so that the system is nearly frequency independent here. Second, for the geometrical dependence of the sensitivity that we are interested in, only the proportionality constant v/D and other possible geometrical parameters of the probe are of relevance.

Since equations (10a) are linear in T , the different components of the source term $\vec{\nabla}T$ in equation (10b) contribute linearly to the perturbation δT . For two parallel wires in free space the output signal (proportional to the temperature difference between the wires) is linearly proportional to the inner product of the vector \vec{v} of the incident gas flow and the vector in the plane of the wires. As noted above, this yields the $\cos \theta$ dependence of the output (the figure-of-eight response). For the current situation, all heated wires and the probe geometry contribute to the temperature distribution around the wires. The output signal of the device, S , thus becomes

$$\begin{aligned} S &= \delta T|_{\text{sensor 1}} - \delta T|_{\text{sensor 2}} \\ &\sim v \partial_x T \cos \theta + v \partial_z T \sin \theta \\ &\sim v(\alpha \cos \theta + \sin \theta), \end{aligned} \quad (11)$$

with $\alpha = \partial_x T / \partial_z T$ the ratio between the x - and z -derivative of the temperature at the place of the wire, averaged over the length of the wire (that is, along y).

The output signal is determined from the two wires in the plane that makes an angle of 45° with the x - y plane, for example the upper-left and lower-right wire in the cross section of figure 2. Ideally, that is if there were no influence of the surrounding device, the polar diagram of the sensitivity would therefore show its maximum at $\theta = 45^\circ$.

One can write for the angular dependence of the temperature difference between these two wires:

$$S(\theta) \sim \alpha \cos \theta + \sin \theta \sim \cos(\theta + \Delta) + \sin(\theta + \Delta), \quad (12)$$

where the angle shift Δ (in radians) is given by

$$\Delta = \arctan \alpha - \pi/4. \quad (13)$$

Thus, the ratio between the x - and z -derivatives of the temperature profile at the wire leads to a θ -independent rotation of the ‘figure of eight’ of the sensitivity in the polar diagram. The maximum sensitivity is shifted from $\theta = 45^\circ$ to $\theta = 45^\circ + \Delta$.

From the expression for the temperature (7) we can easily find its ξ - and ζ -derivatives. These can be evaluated at the

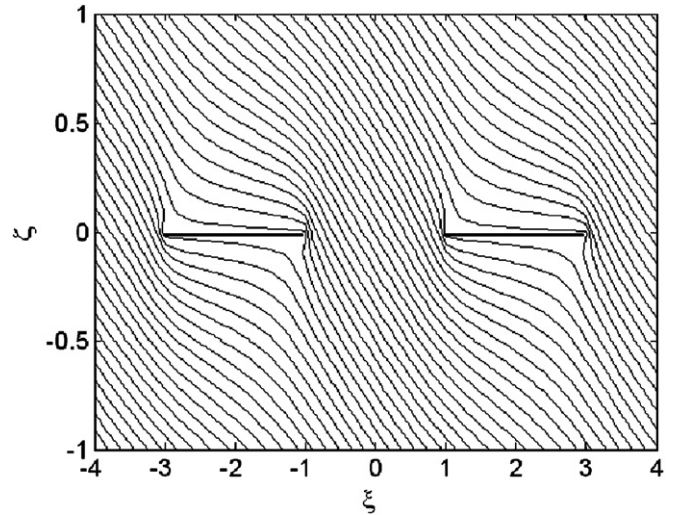


Figure 4. Streamline pattern in the ξ - ζ plane around two thin plates of infinite length in the η -direction, according to the approximate solution based on equation (19). The angle of incidence of the flow is $\pi/8$, the plates have a normalized width 2 and normalized gap distance 2. (So $D = 3 l_x$: $\xi_s = 2$.)

place where a sensor wire is located, $(\xi, \zeta) = (\pm \xi_0, \pm \zeta_0)$. Until now, the sources have been considered as infinitely small (described by delta functions in space). Now, the finite width w and height h of the wires can also be taken into account, by averaging the values for $\partial_\xi T$ and $\partial_\zeta T$ over the wire width and height. With the definitions for the normalized width and height as $\xi_1 = w/2l_x$, $\zeta_1 = h/2l_x$, we calculate these averaged values for $\partial_\xi T$ and $\partial_\zeta T$. After averaging over the wire lengths we obtain for the sensor at $(\xi, \zeta) = (-\xi_0, -\zeta_0)$

$$\begin{aligned} &\frac{1}{8\xi_1\zeta_1} \int_{-\xi_0-\xi_1}^{-\xi_0+\xi_1} d\xi \int_{-1}^1 d\eta \int_{-\zeta_0-\zeta_1}^{-\zeta_0+\zeta_1} d\zeta \partial_\xi T(-\xi_0, \eta, -\zeta_0) \\ &= \sum_{n,m} \frac{P}{kl_y} \frac{(-1)^m}{\lambda_m^2 \sigma_{nm}^2} \sin 2\lambda_n \xi_0 \\ &\times \frac{1 - e^{-\sigma_{nm}\zeta_1} + e^{-2\sigma_{nm}\zeta_0} \sinh \sigma_{nm}\zeta_1}{\zeta_1} \end{aligned} \quad (14a)$$

and

$$\begin{aligned} &\frac{1}{8\xi_1\zeta_1} \int_{-\xi_0-\xi_1}^{-\xi_0+\xi_1} d\xi \int_{-1}^1 d\eta \int_{-\zeta_0-\zeta_1}^{-\zeta_0+\zeta_1} d\zeta \partial_\zeta T(-\xi_0, \eta, -\zeta_0) \\ &= \sum_{n,m} \frac{2P}{kl_y} \frac{(-1)^m}{\lambda_m^2 \sigma_{nm}} \cos^2 \lambda_n \xi_0 \frac{\sin \lambda_n \xi_1}{\lambda_n \xi_1} \\ &\times \frac{e^{-2\sigma_{nm}\zeta_0} \sinh \sigma_{nm}\zeta_1}{\zeta_1}. \end{aligned} \quad (14b)$$

Similar expressions are found for the other wires at the places $(\pm \xi_0, \pm \zeta_0)$.

The ratio between $\partial_\xi T$ and $\partial_\zeta T$ at the wire location determines α and with this value one obtains the angular shift Δ (equation (13)) of the sensitivity. The result is shown in figure 7, where Δ is shown for varying gap distance l_x . As expected, the shift Δ tends to zero for increasing gap distance, which approximates the ‘free space’ geometry.

For the four-wire device under investigation, two different modes of operation can be distinguished. In its normal

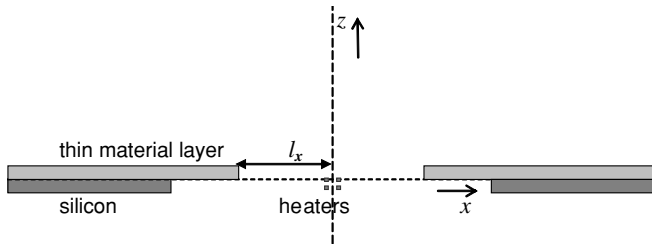


Figure 5. Cross-section of the devices with a thin layer of varying material and varying size on top, that were used in the experiments on the investigation of the temperature effect. The gap distance $2l_x$ was varied in the different designs; the thin top layer was successively balsa wood and silicon.

operation mode, all four wires are heated (equally), as described above with the expansion for the temperature (6), leading to equations (14a) and (14b). A second operation mode is possible, in which only two wires are heated, those placed at an angle of 45° with the x - y plane (for example the upper-left and lower-right heater). To calculate the temperature distribution for this situation, an approach analogous to that described above is followed, by making an expansion in harmonics of the form (6) for the temperature.

Because of the cosine series in the expansion, however, the geometry has to be symmetric in ξ , which is not the case for only two sources at $(\xi, \zeta) = (-\xi_0, \zeta_0)$ and $(\xi, \zeta) = (\xi_0, -\zeta_0)$. We therefore shift one heat source to the origin, make a symmetric expansion, and determine its ξ - and ζ -derivatives for the point at the distance $(\xi, \zeta) = (2\xi_0, 2\zeta_0)$ from the origin. This approximation can be justified when ξ_0 is small.

The resulting value of α for the two-wire case provides us the shift Δ of the polar diagram for this case; it is also depicted in figure 7.

2.2. The air flow imposed on the probe

In section 2.1 it was assumed that the velocity \vec{v} at the point of measurement, at the sensor location, is known, with a local

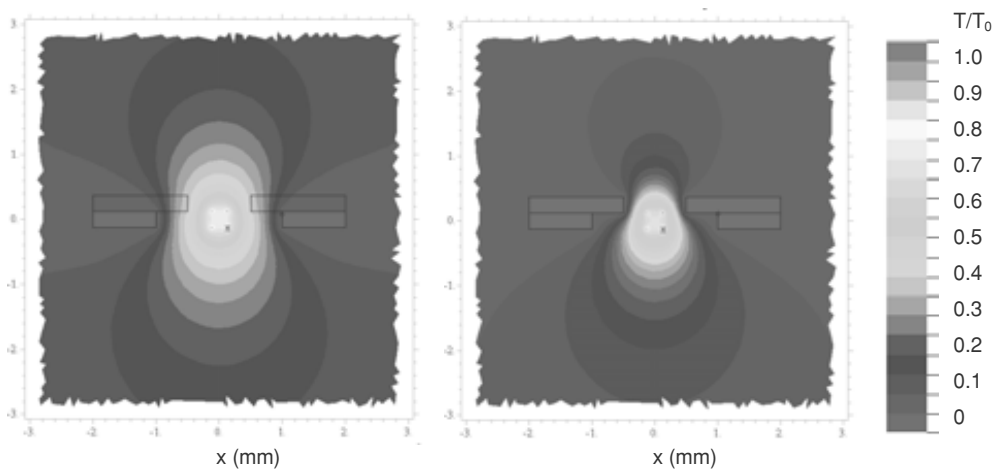


Figure 6. Numerical simulations on the temperature profile in the probe. Shown are cross sections of the chip, on which two thin sheets of material are deposited, displaying the isotherms (normalized by T_0 at the wires). Left: the material has a heat conductivity $k_{\text{air}} = 0.04 \text{ W m}^{-1} \text{ K}^{-1}$ (corresponding to the wood that was used in the experiments); right: with a material having the heat conductivity $k_{\text{si}} = 130 \text{ W m}^{-1} \text{ K}^{-1}$.

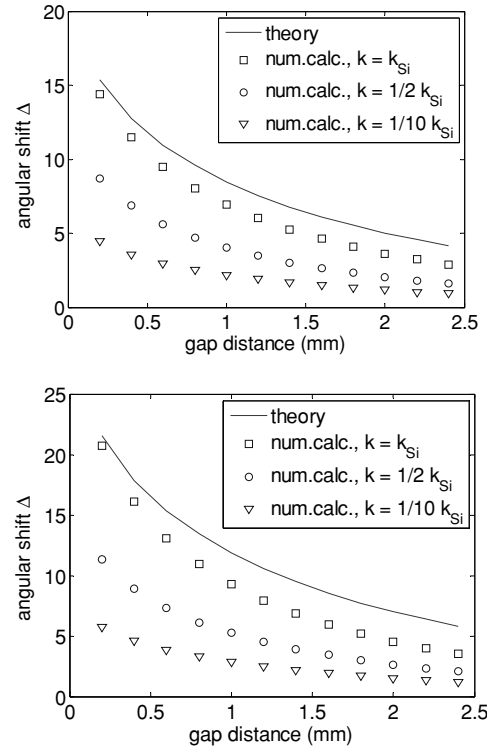


Figure 7. The angular shift Δ as a function of the gap distance according to the numerical simulations of the temperature distribution, for the operation mode with two wires heated (top) and with all four wires heated (bottom). The heat conductivity k of the surrounding probe material was parametrically varied. Also shown is the model prediction for Δ due to the temperature asymmetry according to equations (21).

angle θ with the x - y plane. The influence of the asymmetry of the temperature profile yields then the angle shift Δ of the polar pattern. However, due to the presence of the chip surface the fluid flow itself is influenced as well, and the local angle θ will in general be not the same as the angle of incidence of the acoustic wave far away from the probe. To analyse therefore the air flow around the probe, one should in principle solve the

full Navier–Stokes equations for the three-dimensional probe geometry to obtain the complete particle velocity field around the probe. For the relatively complicated geometry of the real probe as depicted in figure 1, an exact analytic solution cannot be found. Therefore, we model the sensor chip by a pair of long and thin parallel plates, of which the cross section is shown by figure 2, so that the problem becomes two dimensional.

Let us consider first one long, thin sheet of finite width $D-l_x$ and thickness d . Since in general $d \ll (D-l_x)$, we assume the sheet to be infinitely thin and infinitely long. The width is directed along the x -axis, its infinite length along the y -axis and consider the cross section in the x - z plane. We assume a harmonically oscillating acoustic wave with frequency ω and making the angle γ with the x - y plane at infinity. To obtain the flow profile around the plate one should solve the Navier–Stokes equations, the equations of motion for a viscous fluid. Several approximations can be made to solve this two-dimensional problem.

It has been shown [27, 28] that for propagating acoustic waves, the fluid can be considered as incompressible if both the fluid velocity v is small compared to the velocity of sound in the medium, $v \ll c_0$, and the characteristic time scale for velocity changes, $\tau = \omega^{-1}$, is much larger than D/c , that is, if $\tau \gg D/c$. For our case, we can take as estimate values $v \sim 2.5 \times 10^{-3} \text{ m s}^{-1}$ ($\sim 94 \text{ dB}$ sound level), $c_0 = 350 \text{ m s}^{-1}$ and $D = 3 \text{ mm}$, and conclude that for all frequencies well below 10 kHz, both conditions are fulfilled, and the gas can be described as incompressible. For an incompressible fluid, one should solve now the Navier–Stokes equations that read

$$\frac{\partial \vec{v}}{\partial t} + (\vec{v} \cdot \nabla) \vec{v} = -\frac{1}{\rho} \nabla p + \nu \nabla^2 \vec{v}, \quad (15)$$

with \vec{v} the (vectorial) velocity, p the pressure, ν the kinematic viscosity and ρ the fluid density. It was shown before [28] that for the current values of v and these length scales, and $\nu = 1.5 \times 10^{-5} \text{ m}^2 \text{ s}^{-1}$, the nonlinear term in the equation can be neglected. Besides, the equations of motion (15) can be written in terms of a stream function ψ , which is the complex part of the potential and defined by

$$v_x = \frac{\partial \psi}{\partial z}; \quad v_z = -\frac{\partial \psi}{\partial x}. \quad (16)$$

It is then seen [26] that the equation for the stream function to be solved reduces to the Laplace equation

$$\Delta \psi = 0. \quad (17)$$

In this expression for ψ , the time dependence has been eliminated by dividing it by $e^{i\omega t}$. For the two-dimensional geometry in the x - z plane of one infinitely long and thin plate of finite width, the Laplace equation for the stream function can be solved analytically using elliptic coordinates [29]. One can define elliptic coordinates p and q , connected with the normal Cartesian coordinates x, z as $x + iz = c \cosh(p + iq)$, or

$$\begin{aligned} x &= c \cosh p \cos q \\ z &= c \sinh p \sin q \end{aligned} \quad 0 < p < \infty, \quad 0 < q < 2\pi. \quad (18)$$

The curves $p = \text{constant}$ are the ellipses in the x - z plane $x^2/(c^2 \cosh^2 p) + z^2/(c^2 \sinh^2 p) = 1$, while the curves $q = \text{constant}$ are the hyperbolas $x^2/(c^2 \cos^2 q) - z^2/(c^2 \sin^2 q) = 1$, with common foci $(\pm c, 0)$. In this coordinate system, the cross section of the thin plate of width $2c$ is represented by the line extending from $(-c, 0)$ to $(c, 0)$ along the x -axis.

For a fluid velocity having an angle of incidence ϕ at infinity, the solution of equation (17) with the appropriate boundary conditions is then [29]

$$\psi_{\text{oneplate}} = cu_0 \sinh p (\cos \phi \sin q - \sin \phi \cos q). \quad (19)$$

We model our geometry by two parallel long and thin plates, each having a width $D-l_x$ and spaced a distance $2l_x$ apart. Their width is directed along the x -axis, as shown in figure 2. Although this geometry is not analytically solvable anymore, an approximate solution can be composed from a linear combination of two solutions of the form (19) in Cartesian coordinates, mutually shifted over a distance $2D$. This approximation is valid for $l_x \gg (D-l_x)$. We will verify later to what extent this approximation is correct for the current probe dimensions.

Equation (19) is transformed back to Cartesian coordinates, the solution is shifted over $\pm (D + l_x)/2$ and these two functions are added. From the thus obtained stream function the velocities v_x and v_z at the point $\xi = \pm \xi_0$, where the sensors are located, can be determined using (16). Using the normalized variables of section 2.1, these velocities become

$$\begin{aligned} v_x(\xi_0, 0) &= \frac{\partial \psi}{\partial z} = u_0 \cos \phi \\ v_z(\pm \xi_0, 0) &= -\frac{\partial \psi}{\partial x} \\ &= \frac{u_0}{2} \sin \phi \left(\frac{\pm \xi_0 - \xi_s}{\sqrt{(\pm \xi_0 - \xi_s)^2 - (\xi_s - 1)^2}} + \frac{\pm \xi_0 + \xi_s}{\sqrt{(\pm \xi_0 + \xi_s)^2 - (\xi_s - 1)^2}} \right) \end{aligned} \quad (20)$$

where $\xi_s = D/2l_x + 1/2$.

For an angle of incidence $\phi = \pi/8$ and $\xi_s = 2$ the streamline pattern of the solution ψ is illustrated by figure 4. Especially close to the two plates, streamlines are seen to be considerably influenced by the presence of the surfaces.

We can also investigate to what extent the approximation is justified. The sum of two shifted solutions is not exactly a solution of the Laplace equation, equation (19), although the equation is linear. The reason is that the velocity at plate 1 due to the shifted solution of the streamline pattern around plate 2 is no longer tangential to plate 1, a boundary condition that ideally should be fulfilled. Considering the geometry plotted in figure 4, we calculate the y -velocity at $1 < \xi < 3$ due to the contribution to the stream profile related to the left plate (corresponding to the second term in v_z in equation (20)). We find that v_z is below 6% and 2% (at $\xi = 1$ and $\xi = 3$ respectively) of the total velocity at these points. The approximation based on the superposition of two single solutions of the form (19) seems therefore to be justified. For wider gaps the approximation becomes even better.

For the angular shift Δ of the directional sensitivity

$$\Delta = \arctan \alpha - \pi/4, \quad (21)$$

we obtain therefore

$$\alpha = \left(\frac{\xi_0 - \xi_s}{2\sqrt{(\xi_0 - \xi_s)^2 - (\xi_s - 1)^2}} + \frac{\xi_0 + \xi_s}{2\sqrt{(\xi_0 + \xi_s)^2 - (\xi_s - 1)^2}} \right)^{-1}. \quad (22)$$

Equation (22) provides the shift Δ of the sensitivity due to the disturbed fluid flow around the probe. The shift Δ due to the asymmetry in the temperature profile around the wire follows from the equations (11)–(14b). This gives us now all ingredients to compare the model with experimental results. This is accomplished in section 4.

3. Computational fluid dynamics

3.1. The set-up

A commercial finite-volume numerical solver, CFD RC[®] [30, 31], designed for solving linear and nonlinear boundary value problems of partial differential equations, was chosen to analyse the problem.

After division of the volume of interest for the current three-dimensional probe geometry (the solution space) into discrete control volumes or cells and defining the boundary conditions and the initial conditions, the Navier–Stokes equations and heat diffusion equations could be solved numerically at each cell.

To find the heat flow and temperature distribution close to the sensor wires in the probe, a dense and fine grid of very small elements near the wires was required. To determine the air flow around the probe as a whole, a large volume space around the probe is required since the boundary conditions on the incident flow are to be applied ‘at infinity’: far away from the sensors. It was found that solving the complete coupled thermal and flow problem led to unacceptable computation times and memory requirements. We therefore uncoupled the thermal problem of the heat conduction and temperature distribution around the sensor wires, and the air flow problem of the acoustic wave in and around the probe. This approach is justified since it was shown before [12, 26, 28] that the temperature around the wires only affects slightly the viscosity and particle velocity in these regions.

For the three-dimensional heat probe, the solution space was defined as a cylinder of 1 cm length and 1 cm diameter, in which the probe was positioned in the centre. A structured grid of tetrahedral and prismatic volume elements was constructed in the fluid space around the probe. In the region close to the wires, a box of $2 \times 2 \times 1$ mm enclosing the wires, a relatively dense grid was designed with approximately 10 000 cells of typical length $70 \mu\text{m}$. This allowed accurate calculation of the flow through the square orifice and the heat distribution in this region. The geometry of the device as depicted in figure 1 was defined with the real probe dimensions and the actual parameters for the silicon chip, the wires and the air.¹

¹ We took the parameter values $k_{Si} = 130 \text{ W m}^{-1} \text{ K}$, $\rho_{Si} = 2230 \text{ kg m}^{-3}$ and $c_{p,Si} = 702.2 \text{ J kg}^{-1} \text{ K}$ for the silicon chip, $k_{Pt} = 72 \text{ W m}^{-1} \text{ K}$, $\rho_{Pt} = 21090 \text{ kg m}^{-3}$ and $c_{p,Pt} = 133.0 \text{ J kg}^{-1} \text{ K}$ for the platinum wires and $k_{air} = 0.0263 \text{ W m}^{-1} \text{ K}$, $\rho_{air} = 1.16 \text{ kg m}^{-3}$ and $c_{p,air} = 1007 \text{ J kg}^{-1} \text{ K}$ and $\nu_{air} = 1.60 \times 10^{-5} \text{ m}^2 \times \text{s}^{-1}$ for air, at room temperature.

While the device itself was not gridded, the heaters were modelled by approximately 1000 elemental cells of about $20 \times 0.4 \times 0.5 \mu\text{m}$. The outer region around the device as a whole was gridded with 15 000 cells of $\sim 0.4 \text{ mm}$ typical length.

In the flow simulations, we specified a harmonically time varying flow with a fixed velocity and frequency ω . This velocity had a defined angle and magnitude $2 \times 10^{-3} \text{ m s}^{-1}$. These boundary conditions were defined on both the inlets and the outlets. Also, the temperature ($T = 298 \text{ K}$) and pressure (used only to calculate the inlet density, $p = 10^5 \text{ N m}^{-2}$) were specified for each boundary face on these inlets and outlets. The inlets and outlets were formed by the outer surface of the cylindrical volume space. On the surface of the probe, the no-slip boundary condition was applied. To solve the full Navier–Stokes equations several linear equation solvers are available in CFD RC; we used the default conjugate gradient squared solver, with 50 sweeps for the velocity equations and 500 sweeps for the pressure correction equation.

The time dependence of the problem entered via the harmonically changing particle velocity of radial frequency ω . At the boundary faces a plane propagating wave was imposed, with a fluid particle velocity of magnitude u_0 and described by $u(y, t) = u_0 \cos(\omega t - kr)$, with k the wave number in the propagation direction r . The initial condition was formed by the harmonically varying wave at $t = 0$; evaluation of the simulation results was done after the transient values had reached a steady-state situation, about several periods ($\omega t \gg 5$).

For the heat transfer simulations we set the following boundary conditions. On the device surfaces the isothermal heat flux boundary condition in CFD allowed us to fix the temperature at $T = 298 \text{ K}$. At the wire surfaces a specified heat flux of $P = 20 \text{ mW}$ per wire was specified. Also, a convective heat transfer from the wires was defined. This heat flux is not fixed but is calculated from the difference $T_{\text{external}} - T_{\text{wire}}$. We assumed no radiation heat flux.

Heat transfer processes are computed by solving the equation for the conservation of energy. CFD numerically solves the energy equation in the form known as the total enthalpy equation [30, 31]. As argued above, for the frequencies of interest we do not need to take the frequency dependence of the heat processes into account. Therefore, steady-state temperature calculations were done to find the static temperature distribution.

3.2. Calculations on the temperature distribution

Numerical simulations were performed on devices with varying gap distances ($2l_x$ in figure 2), in the range $0.2 \text{ mm} < l_x < 1.8 \text{ mm}$, keeping all other dimensions and parameters the same, and the temperature in the probe, especially close to the heated wires, was evaluated. The fine mesh of small elemental cells ($3\text{--}4 \times 10^{-4} \text{ mm}^3$ in the region close to the wires and 0.1 mm^3 around the device as a whole) allowed for a very accurate determination of the spatial x - and z -derivative of the temperature very close to the wires.

Apart from the variation of the gap distance, the heat conductivity of the chip material was varied, ranging from

the heat conductivity of air, $k_{\text{air}} = 0.0263 \text{ W m}^{-1} \text{ K}^{-1}$, to that of silicon, $k_{\text{Si}} = 130 \text{ W m}^{-1} \text{ K}^{-1}$, in five linear steps. As described in the next section, several probes made of different heat conducting materials were also actually designed (in particular, of wood and of silicon) and to comply with these experiments, those geometries were also analysed in the numerical simulations. The cross section of the experimentally investigated structures as described in section 4, is shown in figure 5; the numerical simulations were performed on the actual geometries of these devices.

The results of the calculations on two suchlike probes are illustrated in figure 6, in which cross sections in the x - z planes containing the isotherms are depicted. The figure shows temperature distributions when all four wires were heated. In figure 3 the calculated temperatures along the lines parallel to the x -, y - and z -axes are also shown, respectively, for $\xi = 0$, $\xi = \xi_0$ and $\xi = 2\xi_0$, and for $\zeta = 0$, $\zeta = \zeta_0$ and $\zeta = 2\zeta_0$. A good agreement with the theoretical prediction for the temperature profiles is seen.

The probe geometry with the cross section as illustrated in figure 5 was analysed for two different modes of operation: one with all four wires heated, dissipating 20 mW heat per wire, and one operation mode in which only the two diagonally placed wires were heated and the other two at room temperature. Both the gap distance and the heat conductivity of the thin sheets on top were varied, the gap distance l_x ranging from 0.2 to 2.4 mm in steps of 0.2 mm, and k between k_{Si} and k_{air} . In figure 7 the results of these numerical calculations for both operation modes are summarized. Shown is the angular shift Δ as a function of the gap distance for various values of k . As a comparison, the model prediction for the angular shift, due to the temperature asymmetry only, is also depicted. It is seen that the theory overestimates the values for Δ for all gap distances. We may attribute this effect to the fact that the theory assumes infinite heat sinks in the z -direction at $x = \pm l_x$, which results in an overestimation of the asymmetry of the temperature profile close to the wires.

3.3. Calculations on the air flow profile

As noted above, the fluid flow profile in the probe was simulated by solving numerically the Navier–Stokes equations for all cells of the solution space, where a plane propagating wave of frequency ω was imposed on the boundary faces of the volume space. In the different simulations, the frequency ω was varied between 0 and 10^4 rad s^{-1} , and the magnitude u_0 was chosen in the range $3 \times 10^{-5} < u_0 < 3 \times 10^{-3} \text{ m s}^{-1}$. Each simulation result provided the magnitude and phase of the particle velocity and the pressure at each point in space, such that the streamline pattern in the fluid could also be investigated. It could be concluded from the results that for the region of interest, $3 \times 10^{-5} < u_0 < 3 \times 10^{-3} \text{ m s}^{-1}$, all dynamics were linear in u_0 , i.e. an increase of the amplitude of the imposed acoustic wave led to an equal increase of the velocities and pressures at all points in space. Therefore, the final calculations were elaborated for one fixed magnitude of u_0 , $u_0 = 2 \times 10^{-3} \text{ m s}^{-1}$.

The angle of incidence ϕ of the applied acoustic wave was varied, and from the magnitude and phase of the calculated

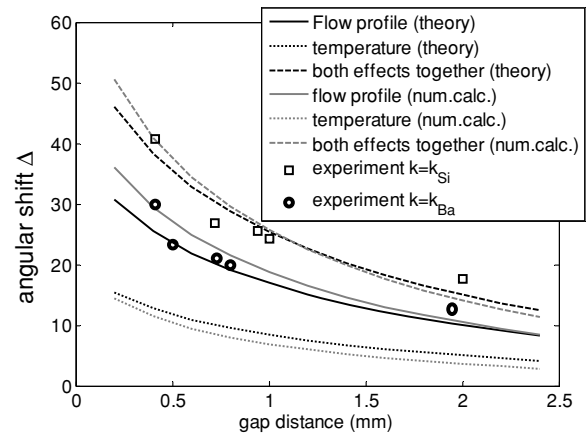


Figure 8. Angular shift as a function of gap distance ($2l_x$) for different types of probes (with balsa wood, and with silicon as surrounding material), and compared with numerical calculations on the devices and with the model predictions. The effects of the temperature, and of the disturbed flow profile, were separately investigated and then added. Simulations on the flow were performed at $u_0 = 2 \times 10^{-3} \text{ m s}^{-1}$, $\omega = 800 \text{ Hz}$.

particle velocity at the sensor location, the angle γ of the local velocity with the horizontal plane was determined. From the difference between the angle γ of the local velocity at the specific point and the angle of incidence ϕ , the deviation $\Delta = \gamma - \phi$ was found. See figure 8. For the readability of the figure, the curves corresponding to the numerical results are represented by lines although the gap distance was varied in discrete steps of 0.2 mm. The results shown in figure 8 refer to a frequency of 800 Hz. Other frequency values in the investigated frequency range ($\omega = 2\pi f$ between 0 and 10^4 rad s^{-1}) did not yield significant differences: curves as plotted in figure 8 for different frequencies cannot be distinguished independently in the figure.

4. Experiments

We built a measurement set-up composed of an approximately 25 cm long standing wave tube [2, 3, 32, 33] of 6 cm width with rigged side walls. At one end, the tube is rigidly terminated with a pressure microphone connected at the tube end; at the other end the air inside is excited by a loudspeaker generating a broadband (frequency 0–10 kHz) signal. Through a small hole in the tube at a 6 cm distance from the sound source, the particle velocity probe is placed in the tube to measure the generated standing wave pattern. From the ratio of the microflown signal and the output of the pressure microphone the sensitivity of the particle velocity sensor could be determined in a frequency range of 10–1000 Hz. The sensor was connected to a step motor, allowing a full rotation in steps of 3.75° .

The measured frequency response was in correspondence with previous measurements on the sensitivity of the particle velocity sensor [13, 24, 26], showing a low-pass frequency response with a roll-off above 2 kHz. The measurement results showed further that the polar pattern of the directional sensitivity was nearly frequency independent in the range from 50 to 1000 Hz for all investigated probes.

To distinguish between the temperature-induced and flow-induced effects, two different kinds of probes were designed.

In one set of probes, silicon was used as the surrounding material around the rectangular orifice in which the wires are suspended. In the other set of probes, the silicon was replaced by a specific type of wood, balsa wood. This type of material was chosen because of its extremely low heat conductivity, $k \approx 0.04 \text{ W m}^{-1} \text{ K}^{-1}$, compared to that of silicon ($k_{\text{Si}} = 130 \text{ W m}^{-1} \text{ K}^{-1}$), thereby being in the order of the thermal conductivity of air ($k_{\text{air}} = 0.0263 \text{ W m}^{-1} \text{ K}^{-1}$). The fabricated designs therefore allowed verification of the hypothesis that the ‘balsa wood’ probes exhibit no temperature-related angular shift of the sensitivity, and that in the silicon-based designs both effects play a role. Each set of probes comprised devices with varying gap distances, with the full gap distance $2l_x$ varying between 0.4 and 2.0 mm.

To determine the angular shift of the sensitivity from the obtained data, the data of the output signal versus angle were fitted by cosine curves using a least mean square optimization routine. These cosine curves were compared with the unshifted cosine functions. The error in the final value for Δ amounted to approximately 3° .

Comprehensive comparison of the results of these measurements with both the numerical simulations and the theoretical calculations is made in figure 8. As the figure shows, the balsa-based probes showed significantly less temperature-related effects, resulting in a smaller angular shift. For these probes, the main reason for the final value of Δ is caused by the flow-induced effects. Besides, this effect is largely dependent on the gap distance of the orifice. The correspondence between the numerical simulations and the experiments is rather good; also the differences between the model predictions and the numerical calculations on the real devices are small.

5. Asymmetric wire placement

From the experiments on the angular sensitivity of the probes it can be concluded that the angular shift Δ is independent of frequency. This means that, for a specific probe geometry of given dimensions, the shift Δ can easily be corrected for, electronically and in the processing of the final output signal, to obtain the ideal ‘figure of eight’ response.

With the obtained theoretic and numerical results one could assume at first sight that an improved geometry can easily be designed, such that the ideal ‘figure-of-eight’ response in the polar plane is obtained. That is, a probe with a maximum sensitivity for incident angles $\theta = 45^\circ$. In such an optimized design, the sensor wires should be placed mutually at an angle in the x - z plane of about $(45 + 18)^\circ$ above each other (when $l_x = 1 \text{ mm}$). Figure 9 shows a cross section of such a probe design. The sensor wires are placed 250 μm above each other (as before) and have a horizontal spacing of 510 μm . The geometry shown in this figure was analysed in the numerical simulations, and the temperature gradients and fluid flow were calculated according to equations (21) and (20).

However, as described in part 1 of the paper, it was observed that such an optimization with respect to the directionality is not achievable. The reason is that the output

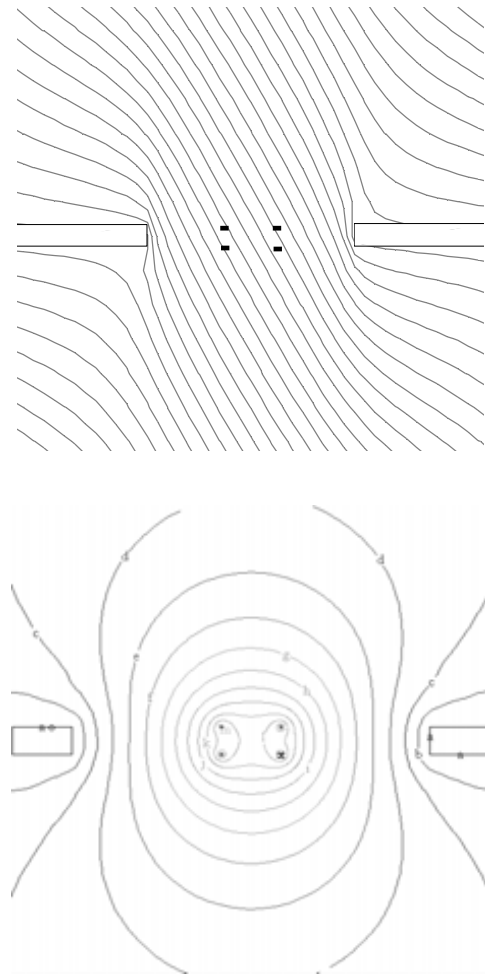


Figure 9. Streamline pattern for an acoustic wave of incident angle $\theta = \pi/4$ (top) and static temperature distribution (bottom) for a design in which the sensor wires are placed at a mutual angle $(45 + 18)^\circ$ in the x - z plane. Dimensions are $l_x = 1.1 \text{ mm}$, $D = 1.2 \text{ mm}$ and wire spacing $510 \mu\text{m}$.

signal (the temperature difference) of two heated wires is dependent on the distance between these wires. Changing the wire spacing therefore influences the temperature difference between the wires. To take this effect into account, one should use the full expression for the temperature difference between two wires, ΔT , as a function of wire spacing a , frequency f and velocity v . The explicit function $\Delta T(f, a, v)$ was deduced before [12, 13, 26]; here in this paper we have only made use of the fact that it is linear in v .

For a full optimization of the current design, the presented model should therefore be refined by incorporating the explicit expression for the two-wire temperature difference. The analytic model contains all the necessary ingredients to realize this. The description of the fluid flow profile does not even change.

6. Conclusions

We analysed the angular sensitivity of the particle velocity probe and obtained analytical expressions for the observed angular shift Δ of the figure-of-eight response using a relatively straightforward model. The model predictions

were compared with numerical results from finite-element calculations and a good agreement between both was found. Two causes of the observed directional dependence of the sensitivity can be distinguished: the asymmetry of the temperature profile around the wires, and the disturbed air flow in the probe, both of which are due to the presence of the chip surface in the proximity of the wires. It was found that the latter effect on Δ is the strongest, and about two times larger than the temperature-induced effect. The analytical model, however, slightly overestimates the influence of the temperature asymmetry.

We performed measurements on the directional sensitivity of various probes of different dimensions and of different heat conducting properties to check the model predictions and the simulations, and these were seen to correspond well. Since the angular sensitivity is nearly frequency independent and Δ is independent of the angle of incidence, this value can relatively easily be corrected for in signal post processing, and the obtained results allow also for an optimized design with an ideal figure-of-eight response.

Acknowledgments

The authors would like to thank the Dutch Technology Foundation (STW) and Microflown technologies B.V. for financial support through the Integrated 3D sound intensity probe project (06407).

References

- [1] Yntema D R, van Honschoten J W and Wiegerink R J 2010 An integrated 3D sound intensity sensor using four-wire particle velocity sensors I: Design and characterization *J. Micromech. Microeng.* **20** 015042
- [2] de Bree H E, Leussink P J, Korthorst M T, Jansen H V, Lammerink T S J and Elwenspoek M 1996 The microflown: a novel device measuring acoustical flows *Sensors Actuators A* **54** 552–7
- [3] de Bree H E 1997 *The Microflown PhD Thesis* University of Twente, The Netherlands (90-36509262)
- [4] de Bree H E, Lammerink T S J, Elwenspoek M C and Fluitman J 1995 Use of a fluid flow-measuring device as a microphone and system comprising such a microphone *Patent PCT/NL95/00220*
- [5] Fahy F J 1995 *Sound Intensity* 2nd edn (London: E&FN SPON)
- [6] Lomas Author C G and Korman M S 1990 Fundamentals of hot wire anemometry *J. Acoust. Soc. Am.* **87** 1379
- [7] Druyvesteyn W F and de Bree H E 2000 A new sound intensity probe; comparison to the Bruel & Kjaer p-p probe *J. Audio Eng. Soc.* **48** 49–56
- [8] Druyvesteyn W F *et al* 1999 A new acoustic measurement probe; the microflown *Proc. of the Institute of Acoustics (London)*
- [9] de Bree H E 2003 An overview of microflown technologies *Acta Acust.* **89** 163–72
- [10] Weyna S 2005 Application of 'microflown' probe to visualization of acoustic power flow *Proc. of the Polish-Scandinavian Struct. Conf. on Acoustic (Poland, 11–15 September)*
- [11] Van Der Eerden F J M, de Bree H E and Tjeldeman H 1998 Experiments with a new acoustic particle velocity sensor in an impedance tube *Sensors Actuators A* **69** 126–33
- [12] Svetovoy V B and Winter I A 2000 Model of the microflown microphone *Sensors Actuators A* **86** 171–81
- [13] van Honschoten J W, Svetovoy V B, Krijnen G J M and Elwenspoek M 2004 Analytic model of a two-wire thermal sensor for flow and sound measurements *J. Micromech. Microeng.* **14** 1468–77
- [14] van Honschoten J W, Yntema D R, Wiegerink R J and Elwenspoek M 2006 Directional sensitivity of a three-dimensional particle velocity sensor *Proc. of MME Conf. (Southampton)* pp 201–4
- [15] van Honschoten J W, Druyvesteyn W F, Kuipers H, Raangs R and Krijnen G J M 2004 Noise reduction in acoustic measurements with a particle velocity sensor by means of a cross-correlation technique *Acta Acust.* **90** 349–55
- [16] Winkel J C, Yntema D R, Druyvesteyn W F and de Bree H E 2006 A particle velocity based method for separating all multi incoherent sound sources *Proc. 31st Fisita World Automotive Congr. (Yokohama, Oct 2006)* (Tokyo: Society of Automotive Engineers of Japan) pp 1–8
- [17] Jacobsen F and Liu Y 2005 Near field acoustic holography with particle velocity transducers *J. Acoust. Soc. Am.* **118** 3139–44
- [18] Nam K-U and Kim Y-H 2001 Visualization of multiple incoherent sources by the backward prediction of near-field acoustic holography *J. Acoust. Soc. Am.* **109** 1808–16
- [19] Visser R 2003 Acoustic source localization based on pressure and particle velocity *Internoise 2003 (Seogwipo, Korea)* N382
- [20] Druyvesteyn W F and Raangs R 2005 Acoustic holography with incoherent sources *Acta Acust.* **91** 932–5
- [21] Raangs R and Druyvesteyn W F 2002 Sound source localization using sound intensity measurement by a three-dimensional PU-probe *112th AES Convention (Munich)*
- [22] Maynard J D, Williams E G and Lee Y 1985 Theory of generalized holography and the development of NAH *J. Acoust. Soc. Am.* **78** 1395–413
- [23] Veronesi W A and Maynard J D 1987 Nearfield acoustic holography (NAH) II: holographic reconstruction algorithms and computer implementation *J. Acoust. Soc. Am.* **81** 1307–22
- [24] Yntema D R, van Honschoten J W, de Bree H E, Wiegerink R J and Elwenspoek M 2006 A three-dimensional microflown *Proc. MEMS (Istanbul)* pp 654–7
- [25] Yntema D R and Druyvesteyn W F 2006 A four particle velocity sensor device *J. Acoust. Soc. Am.* **119** 943
- [26] van Honschoten J W, Yntema D R, Wiegerink R J and Elwenspoek M 2007 Analysis of a three-dimensional particle velocity sensor for design optimization *J. Micromech. Microeng.* **17** S137–46
- [27] Landau L D and Lifschitz E M 2003 *Course of Theoretical Physics vol. 6 Fluid Mechanics* 2nd edn (Oxford: Heinemann, Elsevier)
- [28] van Honschoten J W, Yntema D R, Svetovoy V, Dijkstra M A, Wiegerink R J and Elwenspoek M C 2007 Analysis of the performance of a particle velocity sensor between two cylindrical obstructions *J. Acoust. Soc. Am.* **121** 2711–22
- [29] Lamb H 1975 *Hydrodynamics* 6th edn (Cambridge: Cambridge University Press)
- [30] CFD Research Corporation 2006 Technologies for engineering simulations Huntsville, AL, USA www.cfdrc.com
- [31] Versteeg H and Malalasekera W 1996 *An Introduction to Computational Fluid Dynamics: The Finite Volume Method Approach* (Malaysia: Prentice-Hall)
- [32] Van Der Eerden F J M, de Bree H E and Tjeldeman H 1998 Experiments with a new acoustic particle velocity sensor in an impedance tube *Sensors Actuators A* **69** 126–33
- [33] Van Der Eerden F J M 2001 Noise reduction with coupled prismatic tubes *PhD Thesis* University of Twente, The Netherlands (90-36515211)